Article

Self-Templating Synthesis of 3D Hierarchical NiCo$_2$O$_4$@NiO Nanocage from Hydrotalcites for Toluene Oxidation

Dongdong Wang [1,2], Shuangde Li [1,*], Yingchao Du [1,2], Xiaofeng Wu [1] and Yunfa Chen [1,2,3,*]

[1] State Key Laboratory of Multiphase Complex Systems, Institute of Process Engineering, Chinese Academy of Sciences, Beijing 100190, China; ddwang@ipe.ac.cn (D.W.); ycdu@ipe.ac.cn (Y.D.); xfwu@ipe.ac.cn (X.W.)

[2] University of Chinese Academy of Sciences, No. 19A Yuquan Road, Beijing 100049, China

[3] Center for Excellence in Regional Atmospheric Environment, Institute of Urban Environment, Chinese Academy of Sciences, Xiamen 361021, China

* Correspondence: sdli@ipe.ac.cn (S.L.); yfchen@ipe.ac.cn (Y.C.); Tel.: +86-10-82544896 (Y.C.)

check for updates

Abstract: Rational design LDHs (layered double hydroxides) with 3D hierarchical hollow structures have generated widespread interest for catalytic oxidation due to the high complexity in shell architecture and composition. Herein, we reported a handy two-step method to construct a 3D hierarchical NiCo$_2$O$_4$/NiO nanocage. This synthetic strategy contains a partial in situ transformation of ZIF-67 (zeolitic imidazolate framework-67) into Co-NiLDH yolk-shelled structures following ethanol etching, and a structure-preserved transformation from Co-NiLDH@ZIF-67 to a biphase nanocage following calcination. CoNi-yh-T (varied reaction time and calcination temperature) nanocages were investigated systematically by Brunauer–Emmett–Teller (BET), X-ray photoelectron spectroscopy (XPS), H$_2$- temperature-programmed reduction (TPR), NH$_3$-temperature-programmed desorption (TPD) and studied for toluene oxidation. The CoNi-6h-350 sample showed much higher activity with 90% toluene conversion (T$_{90}$) at 229 °C at a high space velocity (SV = 60,000 mL g^{-1} h^{-1}) than other catalysts (T$_{90}$ >240 °C). Abundant surface high valence Co ions caused by the novel hierarchical nanostructures, together with adsorbed oxygen species and abundant medium-strength surface acid sites, played a key role for catalytic activities.

Keywords: hierarchical nanocage; high surface area; toluene oxidation; lattice defect

1. Introduction

Volatile organic compounds (VOCs), collectively composed by a lot of hazardous organics, not only directly affect environment and human health, but also cause photochemical ozone/smog pollution as precursors [1]. Benzene, toluene, ethylbenzene, and xylenes (BTEX), which are environmentally detrimental VOCs but indispensable chemicals, can corrode skin and irritate the respiratory system, and even affect the nervous system with prolonged exposures [2]. Catalytic oxidation is a promising technology to completely oxidize gas-phase VOCs to carbon dioxide and water with less byproduct [3]. The key point for breaking through the shackles and widely popularizing this technology is to successfully prepare an excellent and low-cost catalyst. Several recent works have demonstrated that transitional mixed metal oxides catalysts have excellent VOCs removal performance because of the merit of increased synergistic effect [4–7]. Besides, surface area, reducibility and adsorbed oxygen species are playing a key role in the design and fabrication of highly efficient mixed metal oxides catalysts for total VOCs oxidation [3,6,8].

Mixed metal oxides catalysts, derived from the calcination of layered double hydroxides (LDHs) precursors, have been widely studied for heterogeneous catalysis, like VOCs oxidation, for some advantages with high dispersion of active components and increased cooperative effect [7,9–12]. Our previous work indicated that mesoporous CoMnAl composited oxides catalysts derived from LDHs show improved benzene oxidation activity because of rich oxygen vacancies [7,13]. However, performance of simple typical structured LDHs is quite limited due to their relatively low surface area which could not adequately expose active sites.

Oxides designed for hierarchical hollow nanostructures with a large surface-to-volume ratio and interconnected pathways for both electrons and ions are of great significance for catalytic oxidation [14–16]. Wang reported template-free scalable synthesis of flower-like $Co_{3-x}Mn_xO_4$ spinel catalysts for toluene oxidation due to rich surface oxygen species over a 3D flower-like structure [17]. Templating-engaged methods employing chemical etching are considered a facile approach, forming hollow structures through the controlled assembly of the desired shells on templates [18]. Porous metal-organic frameworks (MOFs) are normally considered as self-sacrificial templates to synthesize hollow hierarchical nanostrucrues with high surface area and chemical tenability [18,19]. Jiang first reported LDH nanocage synthesized with MOF templates for supercapacitors due to the novel hierarchical structures [20]. Hu designed synthesis of $Co_3O_4/NiCo_2O_4$ double-shelled nanocages through a MOF/LDH framework with better electrocatalytic activity because of the rational design of the hollow structure [14]. However, as we know, the dependence of the hierarchical nanocage catalysts from MOF/LDH for catalytic oxidation VOCs has not been developed.

Co based spinel catalysts with an AB_2O_4 composition and a defect-rich crystal structure, have been reported to be highly active for the catalytic oxidation of hydrocarbons [21]. Herein, Co-NiLDH hierarchical nanopolyhedra are synthesized with zeolitic imidazolate framework-67 (ZIF-67) nanocrystals as the sacrificial template. The reaction time of template etching and the thermal annealing temperature are investigated in detail for the induced textural properties of the as-prepared nanomaterials. Meanwhile, catalytic activities for the degradation of toluene were further investigated to evaluate the role of hierarchical structures.

2. Results and Discussion

2.1. Textural Analysis

The X-ray diffraction (XRD) patterns of ZIF-67, LDH precursors and catalysts are shown in Figure 1. The ZIF-67 XRD pattern is in good agreement with the published result, certifying that we obtained satisfactory ZIF-67 templates [22]. It can be seen from Figure 1a that precursors exhibit a set of peaks (003), (006), (009) and (110), which are classified into hydrotalcite materials, manifest successfully prepared Co-NiLDH [9]. However, different reaction hours have a significant influence on the crystallinity of materials. For example, CoNi-1h-LDH has a low crystallinity, due to insufficient crystal growth time. In addition, we can find characteristic peaks of ZIF-67 ($2\theta = 7.3°, 18.0°, 26.7°, 36.3°$) in Co-NiLDH precursors XRD patterns, which indicated that the constitution of rhombic dodecahedrons ZIF-67 had been retained. Furthermore, the remained ZIF-67 structure can be reconfirmed by precursor scanning electron microscope (SEM) and transmission electron microscope (TEM) images. Then, we calcined Co-NiLDH samples in air and obtained a series oxide samples with their XRD pattern show in Figure 1b. It can be observed that there are still small ZIF-67 characteristic peaks (27.2°) maintaining their existence in oxide catalysts. The diffraction reflections (2θ) at 37.3° (111), 43.4° (200), 63.0° (220) and 75.4° (311) belong to NiO phase (PDF 71-1179). Apart from the above peaks, the strongest reflection at 36.8° (311), together with peaks around 18.9°, 31.3°, 59.2°, and 65.1°, correspond to a $NiCo_2O_4$ spinel phase (PDF 20-0781). However, these peaks can also fit to another spinel oxide phases (Co_3O_4, PDF 42-1467), because there is a little difference between them in diffraction peak intensity and displacement. Fortunately, the real phases of the samples were determined by further analyzing the Raman data.
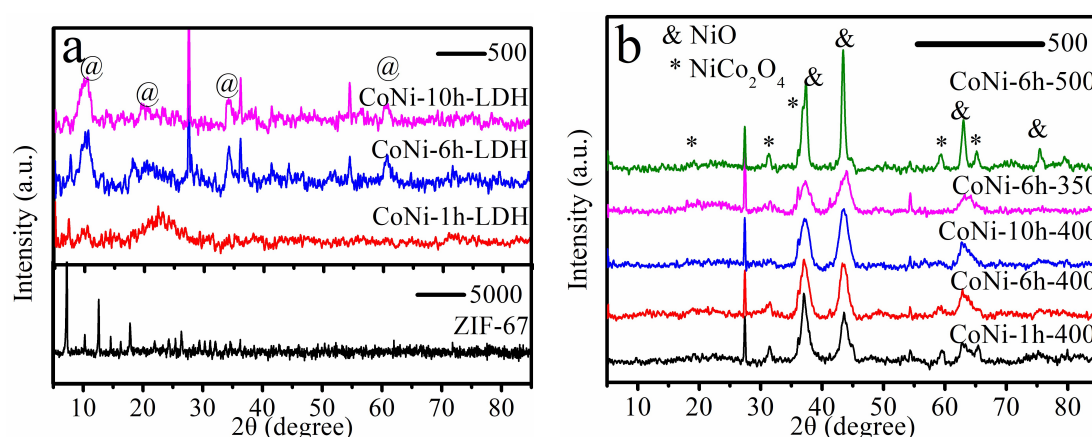
Figure 1. (**a**) X-ray diffraction (XRD) patterns of ZIF-67 and LDH precursors; (**b**) XRD patterns of catalysts.

The reaction system is relatively simple (shown in Figure 2), under the heating and pressure condition, and absolute ethanol triggers Nickel nitrate hexahydrate hydrolysis and ZIF-67 disintegration. Then, Co^{2+}, Co^{3+} and Ni^{2+} ions (O_2 and NO_3^- ions as oxidant participate the Co^{3+} ions formation) form CoNi-LDH nanosheets on the template by co-precipitation [14,20]. The longer heating time, the more the CoNi-LDH nanosheets generation; however, much ZIF-67 structure is simultaneously etched which may lead to hollow structure collapse. Therefore, it is necessary to make a series of heating times as an investigated factor. As illustrated in the Figure 2a SEM image, ZIF-67 single crystals (average size about 500 nm) show a hollow rhombic dodecahedron structure with a well-shaped surface. After hydrothermal treatment shown in Figure 2b,c), the obtained hierarchical Co-NiLDH were adhesively grafted on the ZIF-67 and inherited the polyhedral ZIF-67 structure well. The as-prepared Co-NiLDH, a special 3D hierarchical architecture, are uniformly distributed, nearly perpendicular to the ZIF-67 surface (about 20 nm thickness and several hundreds of nanometers width), and interconnected with each other to form a free-standing irregular mesh configuration. Notably, the ultrathin hollow structure in Figure 3a with plentiful secondary structures can furnish a double sided activity surface and numerous open spaces between neighboring nanosheets to create more catalytically active sites, and exhibit robust catalytic performance. The SEM-energy-dispersive X-ray spectroscopy (EDX) mapping in Figure 4 and Table 1 further indicates the homogeneous distributions of various elements (O, Ni and Co), which make active-element sites highly dispersed. Moreover, the chemical composition of Co-NiLDH determined from EDX is nearly at theoretical values from the initial precursor solutions. After calcination, as shown in Figures 2d–f and 3b–d, the hollow interior and nanosheets structure of the precursor is retained except CoNi-6h-500 catalyst, which consists by a series of small sintered planet. The TEM images and some broken polyhedrons in SEM images clearly indicate the hollow interior of the catalysts. In the selected area electron diffraction (SAED) pattern (Figure 3f–h), the rings at 0.287 nm can be assigned to the (220) spacing of $NiCo_2O_4$, while 0.202 nm matches well with the spacing of the (200) plane of NiO, a further indication the formation of mixed oxide catalysts ($NiCo_2O_4$ and NiO).

The N_2 adsorption/desorption isotherms and pore/size distribution patterns of all samples are shown in Figure 5. The catalyst's surface area and pore volume data, which was obtained using the multipoint Brunauer–Emmett–Teller (BET) method, are shown in Table 1. High specific surface areas (85.5–141.6 m^2 g^{-1}) and rich mesopores structure can be observed, except for the CoNi-6h-500 sample (64.9 m^2 g^{-1} and 0.3 cm^3 g^{-1}). This result further indicated that the catalyst hollow structure was destroyed by high heating temperature. Furthermore, the CoNi-6h-350 sample exhibits a more abundant pore size distribution from 10 nm to 20 nm and the highest surface area (141.6 m^2 g^{-1}), totally provides more catalytically active sites in the toluene reaction.
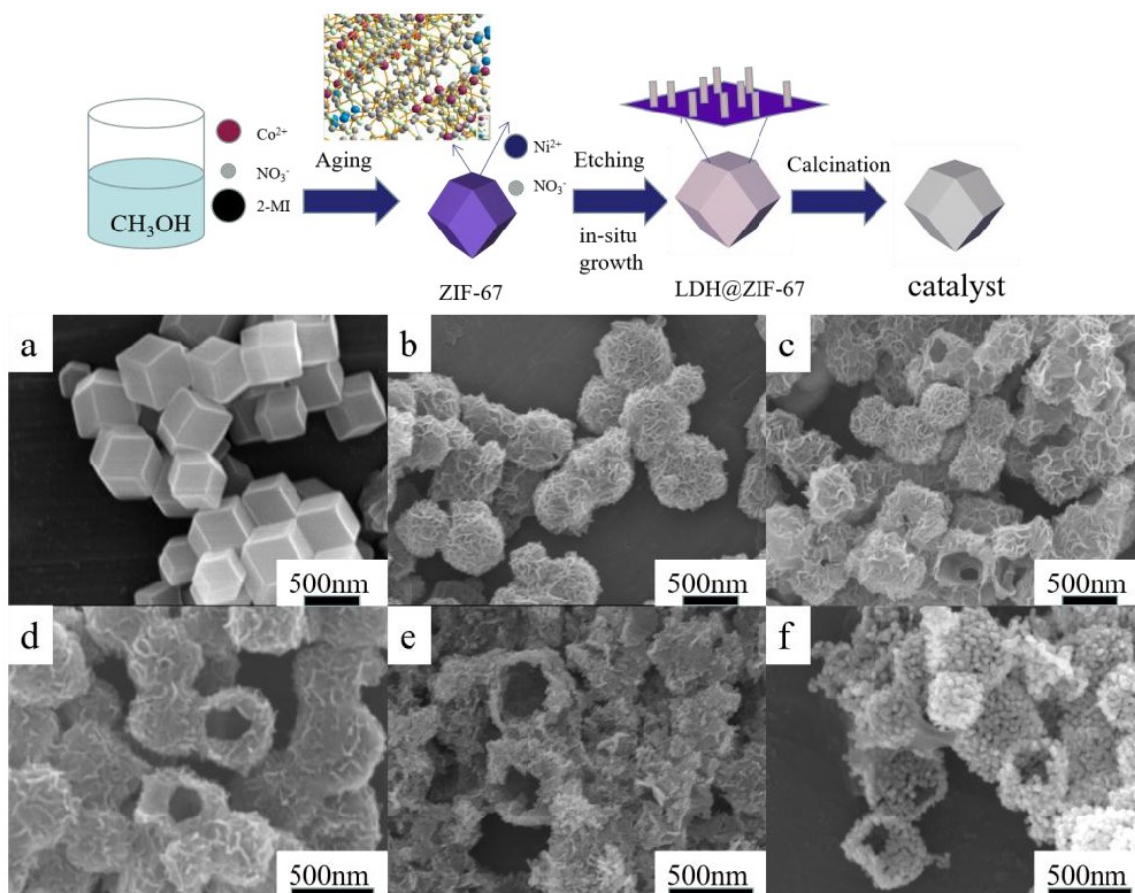
Figure 2. Scheme of synthetic route; (**a–f**) scanning electron microscope (SEM) images of ZIF-67, CoNi-1h-LDH, CoNi-6h-LDH, CoNi-6h-350, CoNi-6h-400, CoNi-6h-500.
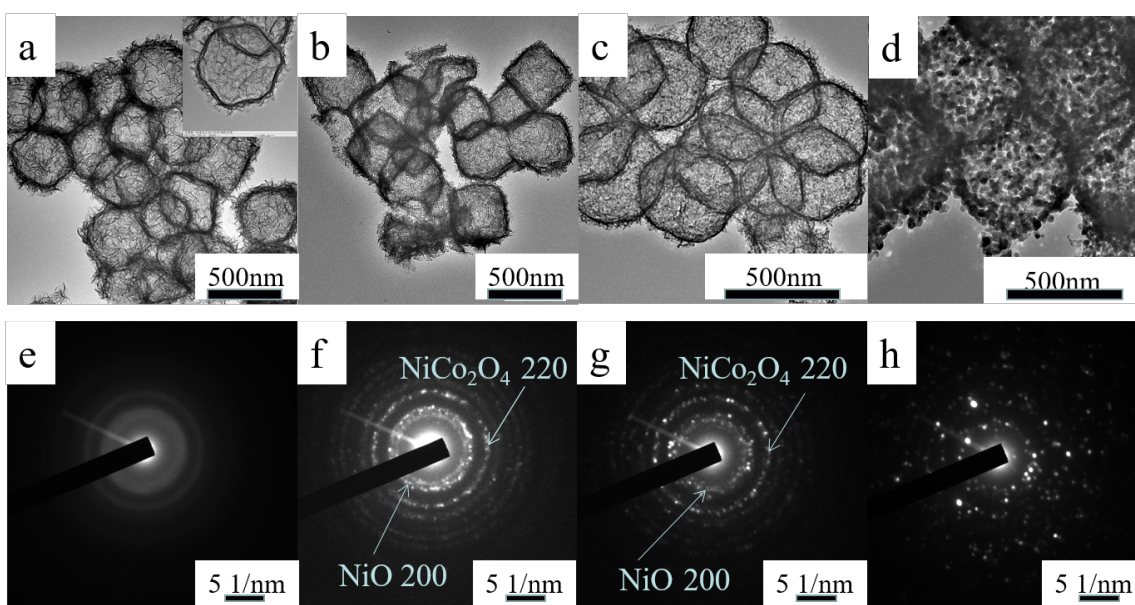

Figure 3. (**a–d**) Transmission electron microscope (TEM) images of CoNi-6h-LDH precursor, CoNi-6h-350, CoNi-6h-400, CoNi-6h-500 catalysts, and (**e–h**) the corresponding SAED pattern in (**a–d**), respectively.
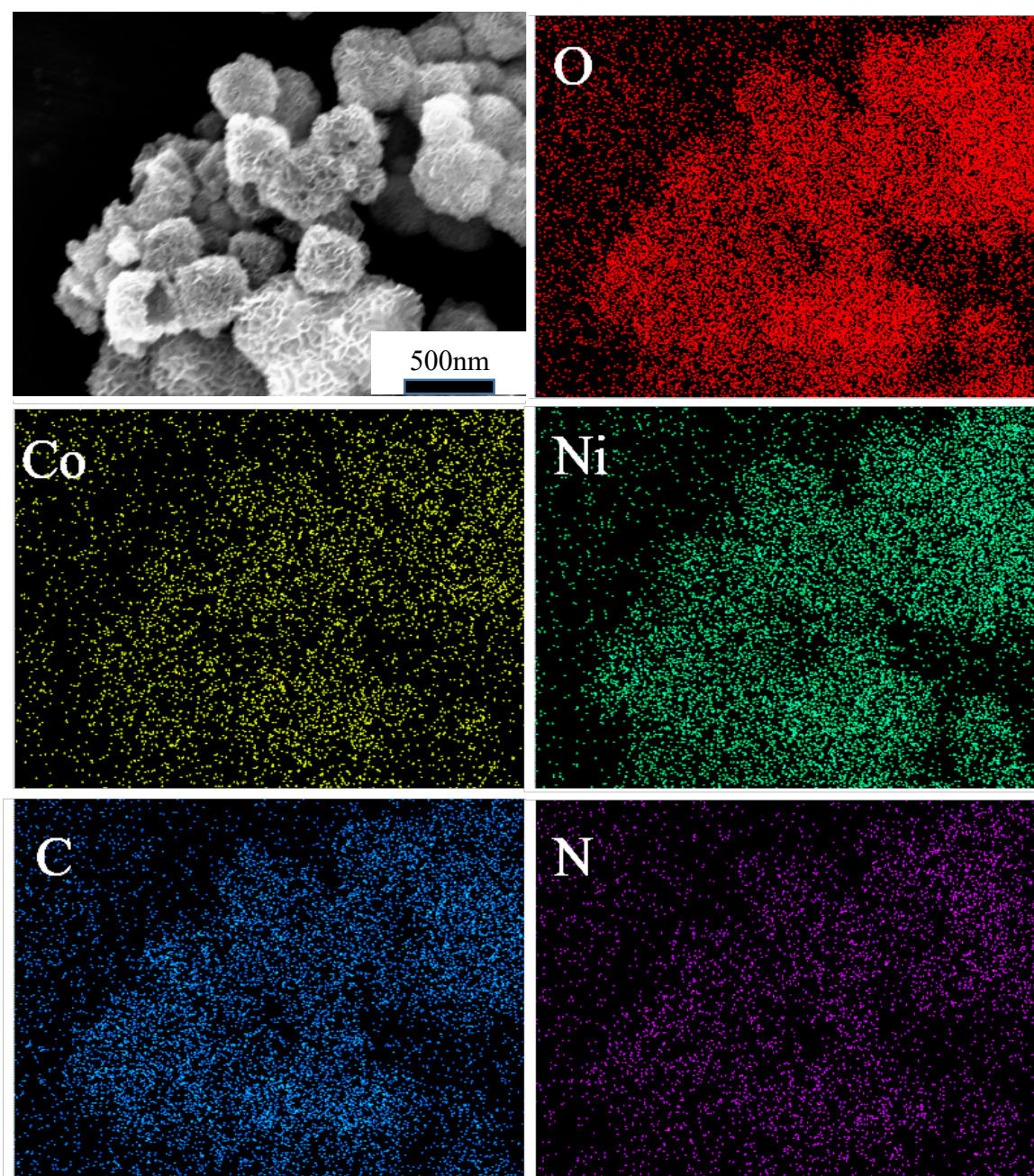
Figure 4. SEM image and element distributions of CoNi-6h-LDH precursor.

Table 1. Physical characterization, catalytic activities, and surface elemental compositions of the samples.

| Sample	BET Surface Area $(m^2\ g^{-1})$	Total Pore Volume $(cm^3\ g^{-1})$	$T_{90}(°C)$	Ni/Co		O_{ads}/O_{latt}	Co^{3+}/Co^{2+}	Quantity of Oxygen Species Based on O2-TPD	Acidity Based on NH_3-TPD
				EDX	XPS				
CoNi-1h-400	85.5	0.66	> 300	2.1	1.1	1.04	0.61	1.095	2.062
CoNi-10h-400	126.3	0.95	259	2.7	2.1	0.90	0.67	1.011	1.730
CoNi-6h-400	98.4	0.67	240	2.0	1.8	1.01	0.82	1.183	1.750
CoNi-6h-350	141.6	0.91	229	2.5	1.9	1.32	1.05	1.185	1.876
CoNi-6h-500	64.9	0.30	244	2.8	1.6	1,30	0.56	0.830	1.343
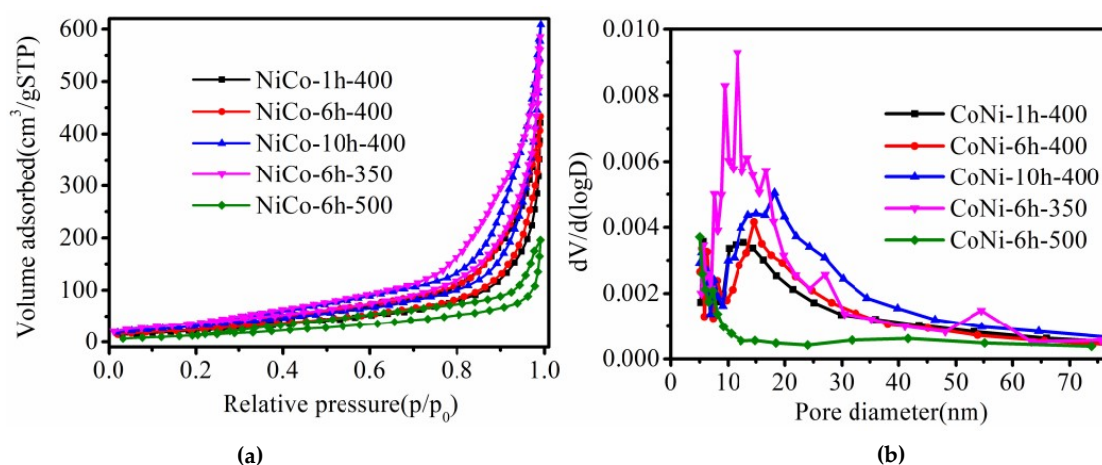
Figure 5. N_2 adsorption-desorption isotherm curves (**a**) and pore size distributions of catalysts (**b**).

2.2. X-ray Photoelectron Spectra (XPS), Raman, Temperature-Programmed Reduction (TPR) and Temperature-Programmed Desorption (TPD)

XPS data reflect the information of catalysts surface element compositions and chemical state, which is indispensable in a catalysis study. The corresponding spectral data were obtained and calibrated based on residual carbon (standard position at 284.6 eV), together with further analysis, and all the results are shown in Figure 6 and Table 1 [23]. The atomic ratio (Ni/Co) of all the samples determined from XPS analysis indicates a quite close ratio to the theoretical chemical composition; however, they are lower than SEM-EDX results to a different extent. The results above indicate that a higher Co species concentration in catalysts surface, which is beneficial for more a active site (Co ions combined with excess Ni ion) fully exposed [24]. In Figure 6a, Co 2p split into two main peaks within 15 eV ($2p_{3/2}$ at 779.6 eV, $2p_{1/2}$ at 794.4 eV) and another two satellite peaks (788.6 eV and 802.6 eV) [25]. According to the Gaussian fitting method, the Co 2p spectrum data can be divided into Co^{3+} peaks, Co^{2+} peaks and three shakeup satellites. The fitting peaks at 779.0 eV, and 794.8 eV are indexed Co^{3+}, and 780.8 eV, and 796.9 eV are ascribed to Co^{2+}. In Figure 6b, Ni 2p spectra has two main peaks ($2p_{3/2}$ at 853.7 eV accompanied with a shoulder, $2p_{1/2}$ at 871.8 eV), with two satellite peak at 860.8 eV, and 879.2 eV. After fitting, Ni^{2+} contains two peaks at 853.9 eV and 870.9 eV, and the peaks at 855.3 eV and 872.7 eV belonged to Ni^{3+}, respectively [26]. The surface Co^{3+}/Co^{2+} proportions are obtained by peak area integral, and the results are summarized in Table 1. Almost all the catalysts maintain a surface Co^{3+}/Co^{2+} ratio of 0.5:0.9, except for CoNi-6h-350 with a ratio of 1.05. The existence of Ni^{3+} in $NiCo_2O_4$ and NiO mixture can be explained by follow mechanism. Ni^{2+} ions occupied the octahedral Co lattice sites, where Co^{3+} was initially present in the $NiCo_2O_4$, which leads to deficiency of positive charges and to maintain charge neutrality, Ni^{2+} transforms to Ni^{3+} [21,27,28]. According to this mechanism, CoNi-6h-350 with a higher Co^{3+}/Co^{2+} ratio demonstrates a relatively intact $NiCo_2O_4$ structure, which is in accordance with the TEM-SEAD. Furthermore, when we increased the calcination temperature of catalysts, more Ni^{2+} ions occupied the octahedral Co lattice sites, and the spinel structure of catalyst destroyed. In Figure 6c, O 1s spectra can be fitted with two peaks: O_{latt} at 529.3 eV which is mainly metal–oxygen bonds, O_{ads} at 530.8 eV which may be surface species and defects, without any other satellite peak [29]. The surface O_{ads}/O_{latt} molar ratio of the CoNi-6h-350 catalyst is 1.32, which is much higher than other samples. This can be explained by the fact that much high valence Co^{3+} existed in CoNi-6h-350 catalyst, induce more surface oxygen vacancies, therefore O_{ads}/O_{latt} ratio higher than other samples. According to previously published studies, especially for the Mars–van Krevelen mechanism, oxygen vacancies (defect) can generate an electropositive catalyst surface, and the electropositive surface will absorb many opposite oxygen units to balance the charge. The electrophilic absorbed oxygen molecules are activated on catalysts surface, and reacts with nucleophilic toluene [30].

Activated adsorbed oxygen, the very beginning species of the benzoquinone reaction route, can totally increase catalyst activity [30,31].
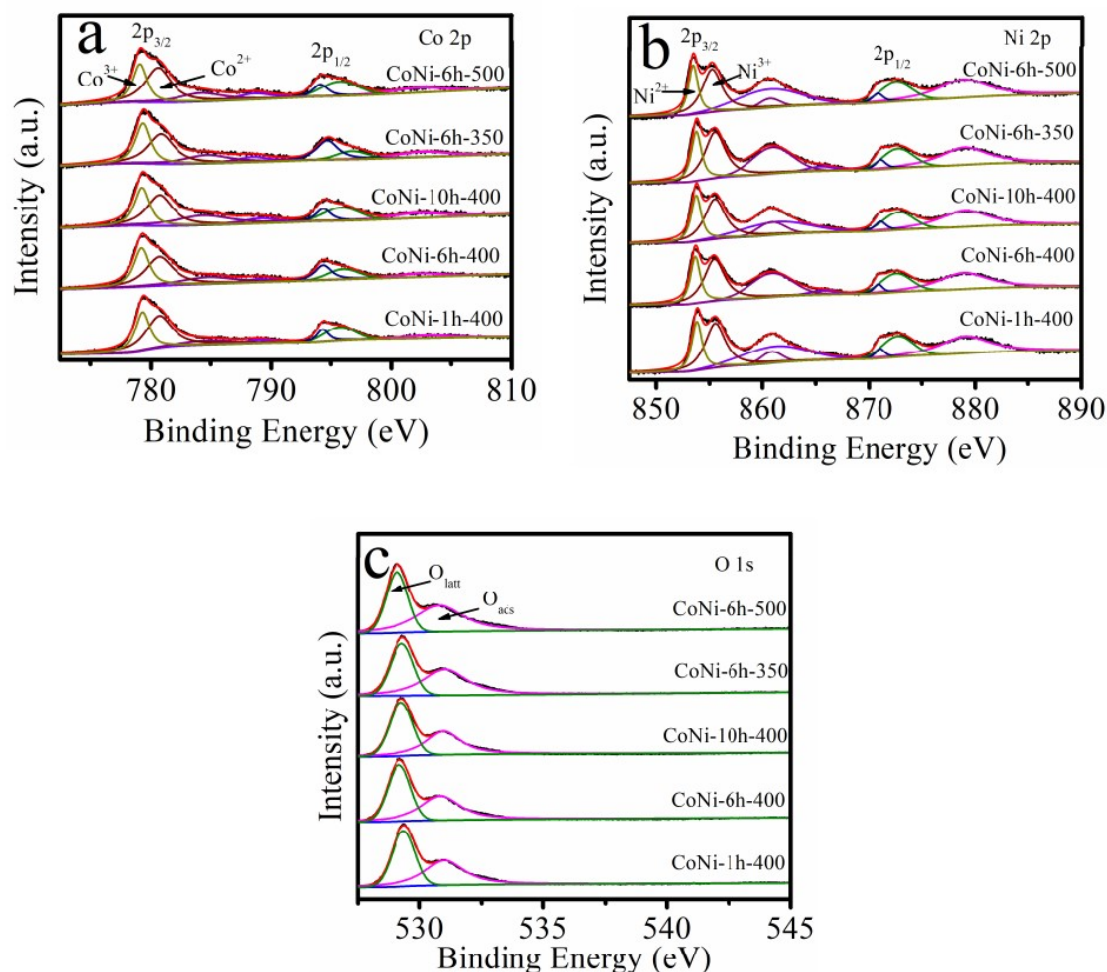

Figure 6. (**a**–**c**) The Co 2p, Ni 2p and O 1s spectra of the catalysts.

The Raman spectrum is a well-recognized, powerful tool for studying defects of nanocrystalline materials. Figure 7a illustrates the Raman spectra of the catalysts which were recorded in the range from 100 to 1800 cm^{-1}. The spectrum principally reveals five peaks located at 125, 348, 506, 651, and 1056 cm^{-1}. The peak at 506 cm^{-1}, which is caused by first-order phonon longitudinal vibration (LO), together with the peak at 1056 cm^{-1} which is caused by second-order phonon longitudinal vibration (2LO), are attributed to NiO characteristic peaks. No observable lateral vibration NiO peaks exist [32]. As can be seen from the spectrum data, the 506 cm^{-1} peak is stronger than 1056 cm^{-1} peak, indicating the NiO structure has defects, because first-order phonon vibration excited by a nickel oxide edge defect but second-order phonon mainly come from the vibration of the complete crystal. $NiCo_2O_4$ is composed by cobalt trivalent, cobalt divalent, and nickel divalent, and has an inverse spinel structure [28,33,34]. Although the characteristic vibration of $NiCo_2O_4$ overlap to NiO at 506 cm^{-1}, the stretching vibration peaks observed at 125, 348 and 651 cm^{-1} are known as $NiCo_2O_4$ vibration for F_{2g}, E_g and A_{1g} [34–36]. So, the Raman results can further identify the phase composition of the catalysts as both NiO and $NiCo_2O_4$, and not Co_3O_4, are included, which cannot be totally confirmed in XRD analysis. Furthermore, no hydroxyl group characteristic peak has been detected, indicating that there is no hydroxide residue after calcinations. The influence of heating hours and calcination temperature on the formation of nanoparticles can be implied from Raman spectrum: the Raman wavenumber values of CoNi-1h-400 are in agreement with NiO, however, $NiCo_2O_4$ are too weak to be correctly

detected; CoNi-6h-350 shows more intense peaks than the other four curves. All these results above are in good agreement with the XRD and SEM results. The CoNi-6h-350 sample exhibit a red shift of about approximately 10 cm^{-1} for LO mode and 5 cm^{-1} for E_g mode, but F_{2g}, A_{1g} and 2LO modes are not affected in comparison with other samples. The red shift can cause by lattice distortion or nanosize effect of nanoparticle, which can induce the formation of oxygen vacancy and enhance the amount of absorbed oxygen species [9].
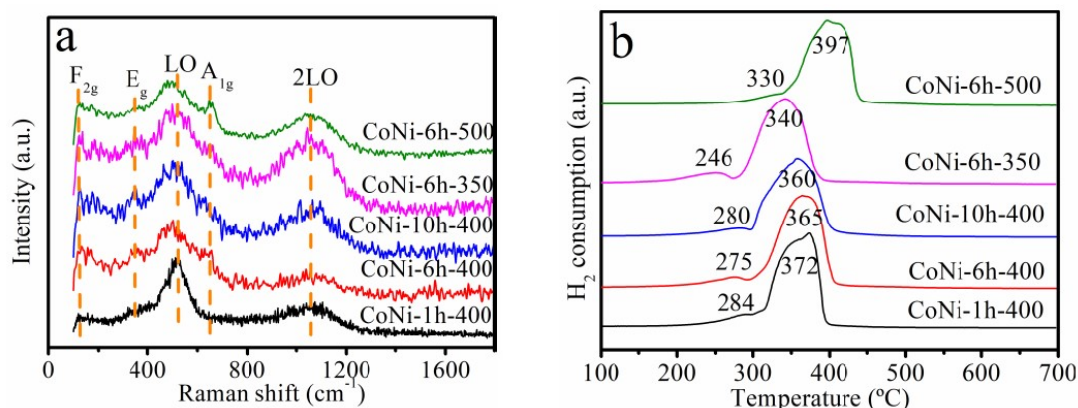

Figure 7. (**a**) Raman spectra profiles of catalysts samples; (**b**) H$_2$- temperature-programmed reduction (TPR) patterns of all the catalyst samples.

The H$_2$-TPR data showed in Figure 7b can reflect catalysts reducibility by analyzing at which temperature hydrogen is oxidized. For each sample, two peaks can been observed, one weak peak at 240–330 °C, another intense peak at 340-400 °C, respectively. During the first peak, NiCo$_2$O$_4$ reacts with hydrogen and become NiCoO$_2$, the second peak is attributed to catalysts totally reduced to nickel and cobalt [37–39]. The first peak temperature is veritable to reflect catalyst reducibility, while the reaction process of the second peak will not happen in an actual toluene removal reaction. The CoNi-6h-350 catalyst, with a richer surface adsorbed oxygen species, has the first reduction temperature at 246 °C (shift to lower temperature at approximately 30 °C), which means it was much more reducible than other samples. Compared with pure Co$_3$O$_4$ whose characteristic peaks are at approximately 352 °C and 674 °C, and pure NiO whose characteristic peak is at approximately 338 °C, NiCo$_2$O$_4$ has a perfect reducibility at low temperature, which is a good argument for synergistic action.

Figure 8a displays the O$_2$-TPD profile of the as-prepared catalysts samples below 700 °C. Three oxygen desorption peaks at different temperatures (145–165 °C, 376–430 °C and 573–700 °C) are observed. With the O$_2$-TPD experiment temperature enhanced, desorption species changed from weak absorbed active oxygen to strongly absorbed lattice oxygen species [21,40]. The desorption peaks at low temperature need to be paid indispensable attention, for active oxygen participates in the toluene removal reaction. However, lattice oxygen species contribute a little to catalytic reaction [29]. Moreover, the content of desorbed oxygen can be quantitatively calculated by integrating the spectrum, and these results can reflect the capacity of the catalysts to accommodate absorbed oxygen species [38,41]. CoNi-6h-350 catalyst has a lower desorption temperature (146 °C and 377 °C as the highest desorption peak) and higher O$_2$ desorption of 1.185 mmol/g than other samples (0.83 mmol/g for CoNi-6h-500), and all of these data are in agreement with the XPS analysis of its high surface adsorbed oxygen species.

To investigate the acid sites type and its concentration of the as-prepared samples, we use NH$_3$-TPD as an effective detecting method, and the data are displayed in Figure 8b. The NH$_3$ desorption peaks can been divided into three parts, below 200 °C corresponded to the weak acid site, and 200–500 °C belongs to the medium-strength acid site, above 500 °C belongs to strong acid site, owing to different NH$_3$ absorption energies on the samples [9,34]. According to the literature, the first peak (<200 °C) is formed by the desorption of physisorbed NH$_3$ and NH$_4^+$ which weak-bonded to surface hydroxyls; the single peak approximately at 430 °C is the desorption of NH$_3$, which is ammonia absorbing on the

Lewis acidic sites; the last broad peak above 500 °C with a shoulder can correspond to the desorption of NH_4^+ which is formed from NH_3 and surface Brønsted acidic sites. Moreover, the concentration of desorbed NH_3 (mmol/g) can reflect well the amount of acid sites in the samples [34,42]. CoNi-6h-350 catalyst with total quantity NH_3 of 1.88 mmol/g and a higher medium-strength acid site at 423 °C may fully accelerate the toluene oxidation because of more capture of electrophilic oxygen molecules on acid site. CoNi-1h-400 sample has an acidity of 2.062, the high quantity can attribute to residual ZIF-67 structure.
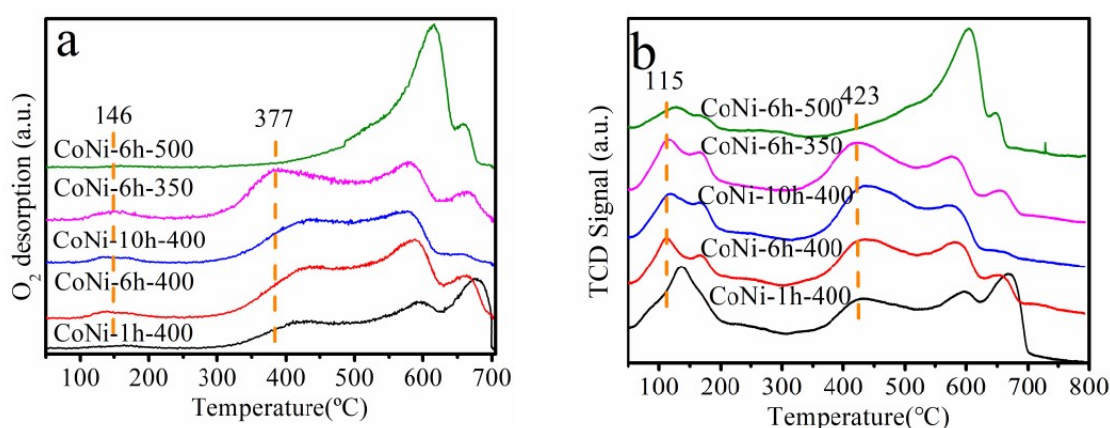

Figure 8. (**a**) O_2-temperature-programmed desorption (TPD) patterns of all the catalysts samples; (**b**) NH_3-TPD patterns of all the catalysts samples.

To further evaluate the texture of the as-prepared catalysts, the XPS spectra (Co 2p, Ni 2p and O 1s) peaks and Raman spectra of CoNi-6h-350 sample before and after the catalytic test are shown in Figure 9. By using a Gaussian fitting method for Figure 9a,b, the Co^{3+}/Co^{2+} ratio decreased from 1.05 to 0.95, which manifests that partial Co^{3+} was reduced during the catalytic process (Co^{3+} to Co^{2+}), while the Ni^{3+}/Ni^{2+} ratio was no significant decline. This indicated that Co^{3+} has a higher activity in the toluene oxidation for the comparison with Ni ion. After the catalytic test, O 1s spectra deconvolve into three components, which is different from fresh catalyst, and the third peak at 533.7 eV is assignable to surface oxygen of hydroxyl species or adsorbed water species. In Figure 9d, Raman spectra shows that 1056 cm^{-1} peak disappeared after the catalytic test; however, other peaks were maintained. The Raman and catalysis results indicating that the crystal texture of nickel oxide being destroyed after catalysis and NiO has a little influence in toluene oxidation, in other words, $NiCo_2O_4$ with synergistic effect provide a better catalytic capacity than NiO.

2.3. Evaluation of the Catalytic Behavior

The catalytic ability of CoNi-yh-T samples for toluene oxidation were evaluated, and the results were shown in Figure 10a. The temperatures of 90% (T_{90}) toluene conversion are summarized in Table 1. The conversion of toluene increased with rising reaction temperature, however, the CO_2 yield has a hysteresis at the beginning of the oxide reaction because of the catalysts inheriting the polyhedral structure of the ZIF-67 template, which possesses a CO_2 adsorption capacity. With the reaction continued, the CO_2 output goes up and the carbon balance reaches 97%; no by-products formed except a minimal CO yield. In contrast with the Co-350 and Ni-350 samples, CoNi-yh-T samples have a better catalytic activity, which demonstrated that synergistic effect has a great effect on catalytic performance. Firstly, we investigated the influence of precursor hydrothermal hours in catalytic activity. The CoNi-6h-400 catalyst exhibited a much higher activity, compared to the CoNi-1h-400 catalyst and CoNi-10h-400; when the hydrothermal reaction time increased, the activity of catalysts first increases, then starts to decrease. Then, we investigated the influence of calcination temperatures. As can been seen, the CoNi-6h-350 sample shows excellent catalytic performance (T_{50} = 220 °C and T_{90} = 229 °C)

for toluene combustion which were 37 °C and >50 °C lower than the worst sample CoNi-1h-400. The excellent activity on the CoNi-6h-350 catalyst can attributed to the retained hollow structure, the high surface area, the rich adsorbed oxygen species, the many medium-strength acid sites, and the low temperature reducibility result from intense synergistic effect, which have been proved by BET, XPS, NH_3-TPD and H_2-TPR, respectively. Moreover, we choose the CoNi-6h-350 sample to continuously catalyze toluene three times with the same experimental conditions to test the reproducibility of the catalysts. As can be seen from the data recorded in Figure 10b, the third cycle of the toluene conversion changes little with T_{90} up to about 10 °C, confirming that it possesses a perfect reproducibility.
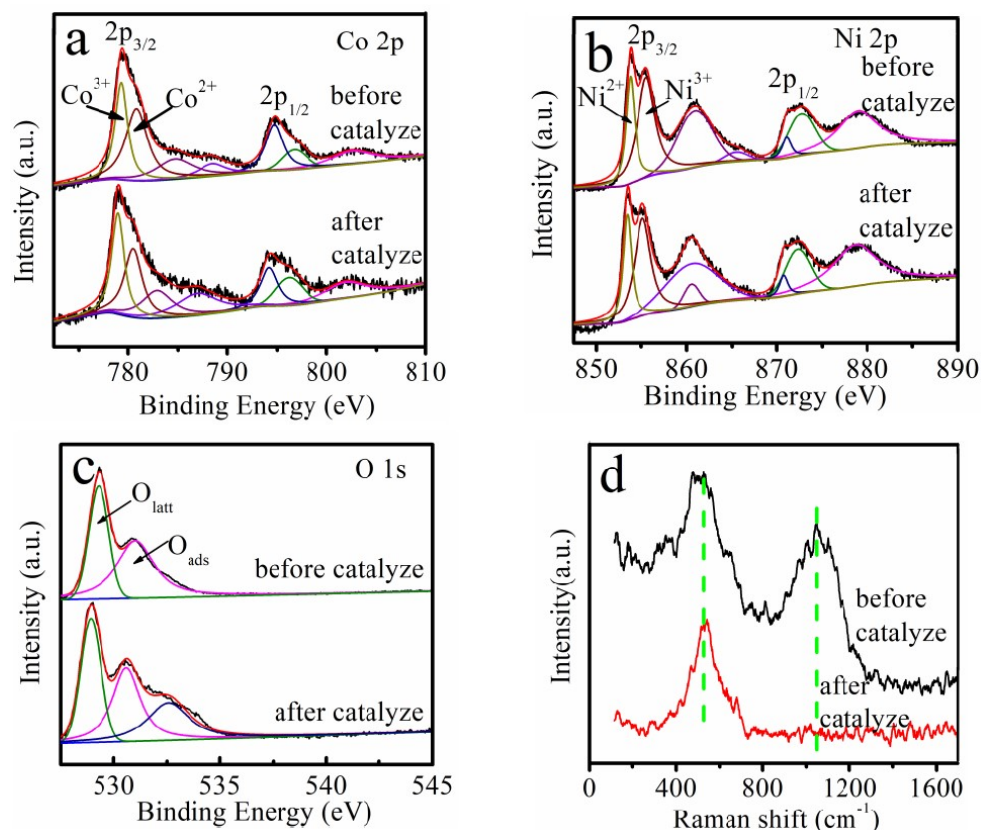

Figure 9. (**a**) Co 2p X-ray photoelectron spectroscopy (XPS) spectra; (**b**) Ni 2p XPS spectra; (**c**) O 1s XPS spectra; (**d**) Raman spectra of the CoNi-6h-350 catalyst before and after the catalytic oxidation reaction.
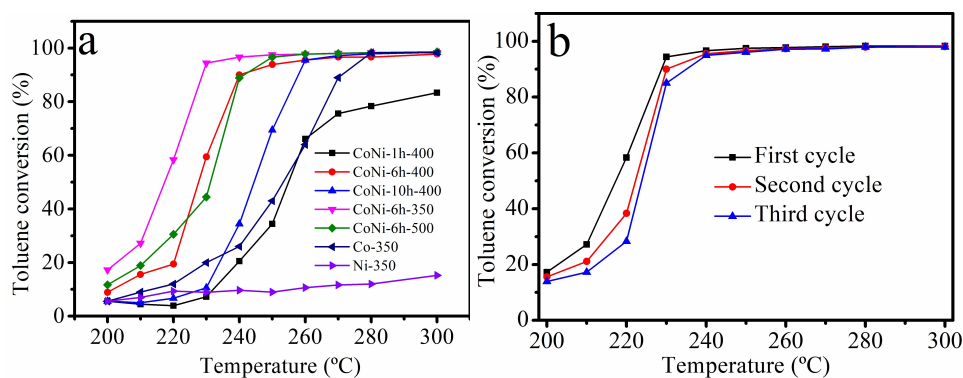

Figure 10. (**a**) toluene conversion as a function of reaction temperature over CoNi-yh-T catalysts under the conditions of toluene concentration 200 ppm in air, SV = 60 000 mL g^{-1} h^{-1}; (**b**) Reproducibility of CoNi-6h-350 catalysts in same condition.

3. Materials and Methods

3.1. Raw Materials and Reagents

Cobalt nitrate hexahydrate (CAS: 10026-22-9), 2-methylimidazole (CAS: 693-98-1, 98%) were obtained from Aladdin. Nickel nitrate hexahydrate (CAS: 13478-00-7, >98%) were obtained from Xilong chemical Co., China. Absolute methanol (99.5%) and ethanol (99.7%) were obtained from Beijing chemical works, China. All these chemicals were used as obtained without further purification.

3.2. Synthesis of ZIF-67

Monodispersed ZIF-67 rhombic dodecahedron were synthesized by following steps: Dissolve 2.91 g $Co(NO_3)_2 \cdot 6H_2O$ and 3.28 g 2-Methylimidazole (2-MIM) in 200 mL anhydrous methanol, separately [19]. Then, 2-MIM solution was quickly added into violently stirred cobalt nitrate solution, and incubated 24 h at 25 °C. Finally, the obtained precipitate was washed with absolute methanol at least three times, and dried at 80 °C overnight.

3.3. Synthesis of Co-NiLDH@ZIF-67

The LDH precursor samples were obtained by the hydrothermal method with a series of different reaction hours. First, 48 mg nickel nitrate hexahydrate and 24 mg ZIF-67 were dissolved in 40 mL ethanol. Then, the mixture was transferred into a Teflon-lined autoclave and its temperature maintained at 120 °C for 1 h, 6 h or 10 h. After that, these samples were washed with absolute ethanol and dried at 80 °C. For the convenience of mark, the obtained samples were named as CoNi-yh-LDH, where y represents the reaction hours.

3.4. Synthesis of $NiCo_2O_4$@NiO Nanocage

CoNi-yh-400 samples were obtained from CoNi-yh-LDH precursors under an air atmosphere calcining process at 400 °C for 4 h (heating rate: 2 °C min^{-1}). Then we selected the best sample among the three CoNi-yh-400 catalysts to consider the influence of calcination temperatures on catalytic power, and obtained two samples denominated CoNi-6h-350, CoNi-6h-500, respectively).

3.5. Synthesis of Single Metal Oxide Catalysts (Co and Ni)

The Co-350 sample was obtained by directly calcining ZIF-67 at 350 °C for 4 h (air atmosphere, heating rate: 2 °C min^{-1}). Moreover, the Ni-350 sample was obtained by calcining nickel foam at same condition.

3.6. Characterization of the Precursors and Catalysts

The powder XRD results were obtained by using Cu-Ka radiation, within a range of scattering angle 2θ of 5–90° (scan rate: 10° min^{-1}). The morphology, microstructures and element distribution of all samples were characterized with a scanning electron microscope (SEM, JEOL JSM-6700F, Japan, 15 kV) and transmission electron microscope (TEM, JEOL JEM-2010F, 200 kV). An automatic surface analyzer (AS-1-C TCD, Quantachrome Cor., USA) and the Brunauer–Emmett–Teller (BET) and Barrett-Joyner-Halenda (BJH) methods were used in BET specific surface area and pore size distribution determination. Each sample had a degassing step at 150 °C for at least 5 h as preprocessing, and then the adsorption-desorption isotherm of N_2 at 77 K was obtained. By using a Renishaw RM2000 Raman Spectrometer, a series of spectrum data (testing rage from 100 to 1500 cm^{-1}) were obtained to further identify the catalysts' structure. X-ray photoelectron spectroscopy (XPS) (XLESCALAB 250Xi electron spectrometer, VG Scientific Co.,) were used to characterize elements species and valence state of the catalysts samples (C 1s peaks at 284.6 eV as the norm of the binding energies of the element). Hydrogen temperature-programmed-reduction (H_2-TPR) results were obtained by using a Quantachrome chemBET pulsar TPR/TPD chemisorption analyzer. The testing processes are as

follows: pretreat catalyst (0.03 g) at 150 °C for 0.5 h with helium flow, then cooling the sample to 25 °C, next heating it to 700 °C (heating rate: 10 °C min^{-1}) with 10.0 vol % hydrogen/argon flow at a rate of 30 mL every minute. The acid types and contents of the samples were tested by using a Micromeritics Instrument Corporation-AutoChem II 2920, which also with a thermal conductivity detector (TCD) and a mass quadrupole spectrometer. 60 mg catalyst was pre-treated at 400 °C with 5% Ammonia/Helium gas flow (50 mL min^{-1}) for 1 h, then cooling to 25 °C and reheating to 700 °C in pure He (50 mL min^{-1}). The temperature-programmed-desorption of oxygen (O$_2$-TPD) with 50 mg catalysts pretreatment in 5% oxygen/helium flow (50 mL min^{-1}) at 400 °C and keep 1 h, then cooling to 25 °C and reheated to 800 °C in pure helium (50 mL min^{-1}).

3.7. Catalytic Activity Measurement

The catalytic activities for totally remove toluene were evaluated in a continuous flow fixed-bed quartz microreactor (i.d. = 6 mm) from 200 to 300 °C with a highly space velocity (SV) at 60,000 mL g^{-1} h^{-1}. For each test process, we add 50 mg catalyst and a little quartz wool into reactor. Toluene was introduced into the reactant flow with its concentration of 200 ppm, and balanced with air (20% O$_2$ + balance N$_2$) at a continuous flow 50 mL min^{-1}. In order to detect the concentration of toluene and CO$_2$, we use a gas chromatograph (Shimadzu GC-2014). Toluene could be detected directly, however, CO$_2$ can only be detected after it changed to CH$_4$. To evaluate the cycle stability of catalysis, one catalyst was measured at same condition for three times.

The conversion of toluene was calculated according to the following equation:

$$\eta \text{toluene} = \frac{C\text{toluene, in} - C\text{toluene, out}}{C\text{toluene, in}} \times 100, \tag{1}$$

$$\eta \text{CO}_2 = \frac{C\text{CO}_2, \text{out}}{7 \times C\text{toluene}} \times 100, \tag{2}$$

where $C_{\text{toluene,in}}$ (ppm), $C_{\text{toluene,out}}$ (ppm) and C_{CO2},out (ppm) are the concentrations of toluene in the inlet and outlet gas, CO$_2$ in the outlet gas, respectively.

4. Conclusions

In summary, a series of hollow-structured catalysts with high surface area and small size have been successfully fabricated by layered double hydroxide@zeolitic imidazolate framework-67 (LDH@ZIF-67) precursors. In order to accurately control the balance between the rates of ZIF-67 template etching and CoNi-LDH formation, we took reaction time into consideration to attain perfect hollow dodecahedral structured precursors. The reaction time and calcination temperature will influence the textural and catalytic properties. The CoNi-6h-350 sample showed 90% toluene conversion (T$_{90}$) at 229 °C at a high space velocity (SV = 60,000 mL g^{-1} h^{-1}), and possessed much higher activity than the CoNi-1h-400 catalyst (T$_{90}$ > 300 °C). The CoNi-6h-350 catalyst exhibited higher catalytic activity because it possessed the largest surface area of 141.6 m^2 g^{-1}, the lowest temperature reducibility, the most abundant surface Co^{3+} and adsorbed oxygen species, and the medium-strength acid site was derived from 3D hierarchical NiCo$_2$O$_4$@NiO nanocage structure.

Author Contributions: Conceptualization, D.W. and S.L.; validation, D.W., Y.D., S.L., X.W. and Y.C.; formal analysis, D.W.; resources, S.L., X.W. and Y.C.; data curation, D.W. and Y.D.; writing—original draft preparation, D.W.; supervision, S.L. and Y.C.; funding acquisition, S.L., X.W. and Y.C.

References

1. Deng, J.; He, S.; Xie, S.; Yang, H.; Liu, Y.; Guo, G.; Dai, H. Ultralow Loading of Silver Nanoparticles on Mn_2O_3 Nanowires Derived with Molten Salts: A High-Efficiency Catalyst for the Oxidative Removal of Toluene. *Environ. Sci. Technol.* **2015**, *49*, 11089–11095. [CrossRef] [PubMed]

2. Genuino, H.C.; Dharmarathna, S.; Njagi, E.C.; Mei, M.C.; Suib, S.L. Gas-Phase Total Oxidation of Benzene, Toluene, Ethylbenzene, and Xylenes Using Shape-Selective Manganese Oxide and Copper Manganese Oxide Catalysts. *J. Phys. Chem. C* **2012**, *116*, 12066–12078. [CrossRef]

3. Zhang, X.; Junhui, Y.; Jing, Y.; Ting, C.; Bei, X.; Zhe, L.; Kunfeng, Z.; Ling, Y.; Dannong, H. Excellent low-temperature catalytic performance of nanosheet Co-Mn oxides for total benzene oxidation. *Appl. Catal. A: Gen.* **2018**, *566*, 104–112. [CrossRef]

4. Tang, W.; Deng, Y.; Li, W.; Li, J.; Liu, G.; Li, S.; Wu, X.; Chen, Y. Importance of porous structure and synergistic effect on the catalytic oxidation activities over hierarchical Mn-Ni composite oxides. *Catal. Sci. Technol.* **2016**, *6*, 1710–1718. [CrossRef]

5. Li, S.; Mo, S.; Li, J.; Liu, H.; Chen, Y. Promoted VOC oxidation over homogeneous porous Co_xNiAlO composite oxides derived from hydrotalcites: Effect of preparation method and doping. *Rsc Advances* **2016**, *6*, S6874–S6884. [CrossRef]

6. Zhai, G.; Wang, J.; Chen, Z.; Yang, S.; Men, Y. Highly enhanced soot oxidation activity over 3DOM Co_3O_4-CeO_2 catalysts by synergistic promoting effect. *J. Hazard. Mater.* **2019**, *363*, 214–226. [CrossRef]

7. Li, S.; Mo, S.; Wang, D.; Wu, X.; Chen, Y. Synergistic effect for promoted benzene oxidation over monolithic CoMnAlO catalysts derived from in situ supported LDH film. *Catal. Today* **2018**. [CrossRef]

8. Li, G.; Zhang, C.; Wang, Z.; Huang, H.; Peng, H.; Li, X. Fabrication of mesoporous Co_3O_4 oxides by acid treatment and their catalytic performances for toluene oxidation. *Appl. Catal. A: Gen.* **2018**, *550*, 67–76. [CrossRef]

9. Mo, S.; Li, S.; Li, J.; Deng, Y.; Peng, S.; Chen, J.; Chen, Y. Rich surface Co(III) ions-enhanced Co nanocatalyst benzene/toluene oxidation performance derived from $Co^{II}Co^{III}$ layered double hydroxide. *Nanoscale* **2016**, *8*, 15763–15773. [CrossRef]

10. Xie, R.; Fan, G.; Yang, L.; Li, F. Solvent-free oxidation of ethylbenzene over hierarchical flower-like core-shell structured Co-based mixed metal oxides with significantly enhanced catalytic performance. *Catal. Sci. Technol.* **2015**, *5*, 540–548. [CrossRef]

11. Liu, Y.; Zhao, J.; Feng, J.; He, Y.; Du, Y.; Li, D. Layered double hydroxide-derived Ni-Cu nanoalloy catalysts for semihydrogenation of alkynes: Improvement of selectivity and anti-coking ability via alloying of Ni and Cu. *J. Catal.* **2018**, *359*, 251–260. [CrossRef]

12. Feng, J.; He, Y.; Liu, Y.; Du, Y.; Li, D. Supported catalysts based on layered double hydroxides for catalytic oxidation and hydrogenation: General functionality and promising application prospects. *Chem. Soc. Rev.* **2015**, *44*, 5291–5319. [CrossRef]

13. Mo, S.; Li, S.; Li, W.; Li, J.; Chen, J.; Chen, Y. Excellent low temperature performance for total benzene oxidation over mesoporous CoMnAl composited oxides from hydrotalcites. *J. Mater. Chem. A* **2016**, *4*, 8113–8122. [CrossRef]

14. Hu, H.; Guan, B.; Xia, B.; Lou, X.W. Designed Formation of Co_3O_4/$NiCo_2O_4$ Double-Shelled Nanocages with Enhanced Pseudocapacitive and Electrocatalytic Properties. *J. Am. Chem. Soc.* **2015**, *137*, 5590–5595. [CrossRef]

15. Sun, C.; Yang, J.; Rui, X.; Zhang, W.; Yan, Q.; Chen, P.; Huo, F.; Huang, W.; Dong, X. MOF-directed templating synthesis of a porous multicomponent dodecahedron with hollow interiors for enhanced lithium-ion battery anodes. *J. Mater. Chem. A* **2015**, *3*, 8483–8488. [CrossRef]

16. Li, Y.; Zhou, F.; Gao, L.; Duan, G. Co_3O_4 nanosheet-built hollow spheres containing ultrafine neck-connected grains templated by PS@Co-LDH. *Sens. Actuators B* **2018**, *261*, 553–565. [CrossRef]

17. Wang, Y.; Arandiyan, H.; Liu, Y.; Liang, Y.; Peng, Y.; Bartlett, S.; Dai, H.; Rostamnia, S.; Li, J. Template-free Scalable Synthesis of Flower-like $Co_{3-x}Mn_xO_4$ Spinel Catalysts for Toluene Oxidation. *ChemCatChem* **2018**, *10*, 3429–3434. [CrossRef]

18. Yang, Q.; Liu, Y.; Xiao, L.; Yan, M.; Bai, H.; Zhu, F.; Lei, Y. Self-templated transformation of MOFs into layered double hydroxide nanoarrays. *Chem. Eng. J.* **2018**, *354*, 716–726. [CrossRef]

19. Yilmaz, G.; Yam, K.M.; Zhang, C.; Fan, H.J.; Ho, G.W. In Situ Transformation of MOFs into Layered Double Hydroxide Embedded Metal Sulfides for Improved Electrocatalytic and Supercapacitive Performance. *Adv. Mater.* **2017**, *29*. [CrossRef] [PubMed]

20. Jiang, Z.; Li, Z.; Qin, Z.; Sun, H.; Jiao, X.; Chen, D. LDH nanocages synthesized with MOF templates and their high performance as supercapacitors. *Nanoscale* **2013**, *5*, 11770–11775. [CrossRef] [PubMed]

21. Ren, Z.; Botu, V.; Wang, S.; Meng, Y.; Song, W.; Guo, Y.; Ramprasad, R.; Suib, S.L.; Gao, P.X. Monolithically integrated spinel $M_xCo_{3-x}O_4$ (M = Co, Ni, Zn) nanoarray catalysts: Scalable synthesis and cation manipulation for tunable low-temperature CH_4 and CO oxidation. *Angew. Chem. Int. Ed. Engl.* **2014**, *53*, 7223–7227. [CrossRef]

22. Li, R.; Che, R.; Liu, Q.; Su, S.; Li, Z.; Zhang, H.; Liu, J.; Liu, L.; Wang, J. Hierarchically structured layered-double-hydroxides derived by ZIF-67 for uranium recovery from simulated seawater. *J. Hazard. Mater.* **2017**, *338*, 167–176. [CrossRef]

23. Demchenko, I.N.; Syryanyy, Y.; Melikhov, Y.; Nittler, L.; Gladczuk, L.; Lasek, K.; Cozzarini, L.; Dalmiglio, M.; Goldoni, A.; Konstantynov, P.; et al. X-ray photoelectron spectroscopy analysis as a tool to assess factors influencing magnetic anisotropy type in Co/MgO system with gold interlayer. *Scripta Mater.* **2018**, *145*, 50–53. [CrossRef]

24. Zhao, C.; Wu, J.; Yang, L.; Fan, G.; Li, F. In Situ Growth Route to Fabricate Ternary Co–Ni–Al Mixed-Metal Oxide Film as a Promising Structured Catalyst for the Oxidation of Benzyl Alcohol. *Ind. Eng. Chem. Res.* **2017**, *56*, 4237–4244. [CrossRef]

25. Lv, Z.; Zhong, Q.; Bu, Y. Controllable synthesis of Ni-Co nanosheets covered hollow box via altering the concentration of nitrate for high performance supercapacitor. *Electrochim. Acta* **2016**, *215*, 500–505. [CrossRef]

26. Tian, X.; Tian, C.; Nie, Y.; Dai, C.; Yang, C.; Tian, N.; Zhou, Z.; Li, Y.; Wang, Y. Controlled synthesis of dandelion-like $NiCo_2O_4$ microspheres and their catalytic performance for peroxymonosulfate activation in humic acid degradation. *Chem. Eng. J.* **2018**, *331*, 144–151. [CrossRef]

27. Shao, J.; Wan, Z.; Liu, H.; Zheng, H.; Gao, T.; Shen, M.; Qu, Q.; Zheng, H. Metal organic frameworks-derived Co_3O_4 hollow dodecahedrons with controllable interiors as outstanding anodes for Li storage. *J. Mater. Chem. A* **2014**, *2*, 12194–12200. [CrossRef]

28. Bhaway, S.M.; Tangvijitsakul, P.; Lee, J.; Soucek, M.D.; Vogt, B.D. High rate sodium ion battery anodes from block copolymer templated mesoporous nickel–cobalt carbonates and oxides. *J. Mater. Chem. A* **2015**, *3*, 21060–21069. [CrossRef]

29. Su, L.; Dong, W.; Wu, C.; Gong, Y.; Zhang, Y.; Li, L.; Mao, G.; Feng, S. The peroxidase and oxidase-like activity of $NiCo_2O_4$ mesoporous spheres: Mechanistic understanding and colorimetric biosensing. *Anal. Chim. Acta* **2017**, *951*, 124–132. [CrossRef]

30. Li, K.; Chen, J.; Bai, B.; Zhao, S.; Hu, F.; Li, J. Bridging the reaction route of toluene total oxidation and the structure of ordered mesoporous Co_3O_4: The roles of surface sodium and adsorbed oxygen. *Catal. Today* **2017**, *297*, 173–181. [CrossRef]

31. Liao, Y.; Zhang, X.; Peng, R.; Zhao, M.; Ye, D. Catalytic properties of manganese oxide polyhedra with hollow and solid morphologies in toluene removal. *Appl. Surf. Sci.* **2017**, *405*, 20–28. [CrossRef]

32. Anandha Babu, G.; Ravi, G.; Hayakawa, Y. Microwave synthesis and effect of CTAB on ferromagnetic properties of NiO, Co_3O_4 and $NiCo_2O_4$ nanostructures. *Appl. Phys. A* **2014**, *119*, 219–232. [CrossRef]

33. Liotta, L.F.; Wu, H.; Pantaleo, G.; Venezia, A.M. Co_3O_4 nanocrystals and Co_3O_4–MO_x binary oxides for CO, CH_4 and VOC oxidation at low temperatures: A review. *Catal. Sci. Technol.* **2013**, *3*, 3085–3102. [CrossRef]

34. Cai, X.; Sun, W.; Xu, C.; Cao, L.; Yang, J. Highly selective catalytic reduction of NO via SO_2/H_2O-tolerant spinel catalysts at low temperature. *Environ. Sci. Pollut. Res. Int.* **2016**, *23*, 18609–18620. [CrossRef]

35. Wang, B.; Cao, Y.; Chen, Y.; Wang, R.; Wang, X.; Lai, X.; Xiao, C.; Tu, J.; Ding, S. Microwave-assisted fast synthesis of hierarchical $NiCo_2O_4$ nanoflower-like supported $Ni(OH)_2$ nanoparticles with an enhanced electrocatalytic activity towards methanol oxidation. *Inorg. Chem. Frontiers* **2018**, *5*, 172–182. [CrossRef]

36. Mazzi, A.; Bazzanella, N.; Orlandi, M.; Edla, R.; Patel, N.; Fernandes, R.; Miotello, A. Physical vapor deposition of mixed-metal oxides based on Fe, Co and Ni as water oxidation catalysts. *Mater. Sci. Semicond. Process.* **2016**, *42*, 155–158. [CrossRef]

37. Wang, X.; Wen, W.; Mi, J.; Li, X.; Wang, R. The ordered mesoporous transition metal oxides for selective catalytic reduction of NO_x at low temperature. *Appl. Catal. B: Environ.* **2015**, *176–177*, 454–463. [CrossRef]

38. Rouibah, K.; Barama, A.; Benrabaa, R.; Guerrero-Caballero, J.; Kane, T.; Vannier, R.-N.; Rubbens, A.; Löfberg, A. Dry reforming of methane on nickel-chrome, nickel-cobalt and nickel-manganese catalysts. *Int. J. Hydrogen Energy* **2017**, *42*, 29725–29734. [CrossRef]

39. Bai, G.; Dai, H.; Deng, J.; Liu, Y.; Qiu, W.; Zhao, Z.; Li, X.; Yang, H. The microemulsion preparation and high catalytic performance of mesoporous NiO nanorods and nanocubes for toluene combustion. *Chem. Eng. J.* **2013**, *219*, 200–208. [CrossRef]

40. Tang, C.-W.; Wang, C.-B.; Chien, S.-H. Characterization of cobalt oxides studied by FT-IR, Raman, TPR and TG-MS. *Thermochim. Acta* **2008**, *473*, 68–73. [CrossRef]

41. Wang, Y.; Guo, L.; Chen, M.; Shi, C. CoMn$_x$O$_y$ nanosheets with molecular-scale homogeneity: An excellent catalyst for toluene combustion. *Catal. Sci. Technol.* **2018**, *8*, 459–471. [CrossRef]

42. Zhou, K.; Mousavi, B.; Luo, Z.; Phatanasri, S.; Chaemchuen, S.; Verpoort, F. Characterization and properties of Zn/Co zeolitic imidazolate frameworks vs. ZIF-8 and ZIF-67. *J. Mater. Chem. A* **2017**, *5*, 952–957. [CrossRef]